

Processing and optical behavior of dense (Hf,Zr)B₂ solid solutions for solar energy receivers

Simone Barbarossa^a, Antonio M. Locci^a, Giacomo Cao^a, Sebastiano Garroni^b, Andrea Balbo^c, Federica Zanutto^c, Elisa Sani^{d,*}, Roberto Orrù^a

^a Dipartimento di Ingegneria Meccanica, Chimica, e dei Materiali, Unità di Ricerca del Consorzio Interuniversitario Nazionale per la Scienza e Tecnologia dei Materiali (INSTM), Università degli Studi di Cagliari, via Marengo 2, 09123, Cagliari, Italy

^b Dipartimento di Scienze Chimiche, Fisiche, Matematiche e Naturali, Università degli Studi di Sassari, 07100, Sassari, Italy

^c Corrosion and Metallurgy Study Centre "Aldo Daccò", Engineering Department, University of Ferrara, G. Saragat 4a, Ferrara, 44122, Italy

^d CNR-INO National Institute of Optics, Largo E. Fermi, 6, I-50125, Firenze, Italy

ARTICLE INFO

Keywords:

Solid solution
Borides
Spark plasma sintering
Optical properties
Solar absorbers
Concentrated solar power

ABSTRACT

While individual borides and, more recently, quinary High Entropy Transition Metal Borides have been investigated, the fabrication and characterization of bulk binary to quaternary solid solutions are barely explored. In this work, dense (Hf_{0.5}Zr_{0.5})B₂ is produced by Spark Plasma Sintering (SPS) from powders prepared by Self-propagating High-temperature (SHS). SHS produced a multiphase product, whose secondary phases are fully converted into the desired diborides during the subsequent SPS step. Optical properties of (Hf_{0.5}Zr_{0.5})B₂ are evaluated for the first time with focus on the possible use as novel high-temperature solar thermal absorber, by hemispherical reflectance measurements and calculation of solar absorptance, temperature-dependent spectral selectivity and absorber opto-thermal efficiency at various solar concentration ratios. To optimize the material, a chemically etched surface texture was realized to modify the optical properties. The etched sample showed a higher solar absorptance (0.71) and a lower spectral selectivity than the unetched one, with consequent higher opto-thermal efficiency at all temperatures for solar concentration ratios 1000 ÷ 3000, while at lower concentration ratios and temperatures >1400 ÷ 1600 K, the unetched sample shows the highest efficiency. These results show the promising properties of binary diborides for solar thermal applications.

1. Introduction

Due to their highly refractory nature, with melting points exceeding 3200 °C, and other attractive physico-chemical properties (high hardness, thermal stability, resistance to corrosion, chemical inertness, good electrical conductivity, intrinsic spectral selectivity, etc.), zirconium and hafnium diborides are the most representative and investigated members of Ultra High Temperature Ceramics (UHTCs) [1,2]. Such characteristics make them suitable for use under harsh conditions, such as in the aerospace industry (thermal protection systems) [2], but also in other emerging application fields, like solar energy [3,4].

By considering the high mutual solubility displayed by Zr- and Hf-diborides, the latter have been also combined in different proportions to form thermodynamically stable (Hf_xZr_{1-x})B₂ solid solutions [5–16]. The methods proposed in the literature for their synthesis are chemical vapor deposition (CVD) [5,6], arc-melting [9], mechanically induced

self-sustaining reaction [10], heat treatment of co-ball milled ZrB₂ and HfB₂ powders [11–14], molten salt route [15,16], carbothermal (CTR) and borohydride (BHR) reduction followed by flash sintering [7], and microwave co-assisted boro/carbothermal reduction [8]. Only few of them [7,11–14] were addressed to the obtainment of bulk ceramics. McClane et al. [11] produced 99.5% dense (Zr_{0.97}Hf_{0.03})B₂ solid solutions by a multi-step hot pressing procedure (dwell temperature up to 2150 °C), from ball milled ZrB₂, HfB₂, and graphite powders. Individual borides were also used by Sitler et al. [12–14] as precursors for the preparation of bulk (Hf_xZr_{1-x})B₂, with x = 0.2, 0.5, and 0.8. Initial powders were first ball milled for 3 h (ball to powder mass ratio equal to 10) and subsequently processed for 10 min by Spark Plasma Sintering (SPS) at 1700 °C, under vacuum conditions. The resulting sintered products displayed relative densities equal to 82.9 (x = 0.2), 76.2 (x = 0.5), and 76.5% (x = 0.8), and consisted of the expected solid solutions, with HfO₂ also detected by XRD analysis [12,13]. Among the three compositions investigated, (Hf_{0.5}Zr_{0.5})B₂ samples showed the best

* Corresponding author.

E-mail address: elisa.sani@ino.cnr.it (E. Sani).

<https://doi.org/10.1016/j.solmat.2024.112755>

Received 5 October 2023; Received in revised form 4 January 2024; Accepted 7 February 2024

Available online 19 February 2024

0927-0248/© 2024 The Authors. Published by Elsevier B.V. This is an open access article under the CC BY license (<http://creativecommons.org/licenses/by/4.0/>).

Meaning of abbreviations

APS	Average Particle Size
BHR	Borohydride reduction
CVD	chemical vapor deposition
CTR	Carbothermal reduction
DSC	Differential Scanning Calorimetry
DTA	Differential Thermal Analysis
EDX	Energy Dispersive X-ray Analysis
FT-IR	Fourier Transform InfraRed
HEBs	High entropy diborides
SEM	Scanning Electron Microscopy
SHS	Self-propagating High-temperature Synthesis
SPS	Spark Plasma Sintering
UHTCs	Ultra High Temperature Ceramics
TGA	Thermogravimetric Analysis
XRD	X-Ray Diffraction

corrosion resistance [12], and electrocatalytic properties [13]. Furthermore, the CTR and BHR routes were compared by Belisario et al. [7] for the preparation of $(\text{Hf}_{0.5}\text{Zr}_{0.5})\text{B}_2$ powders to be consolidated by Flash Sintering. In the latter study, the oxidation behavior of the obtained 70% (CTR) and 95% (BHR) dense samples was compared by TGA-DSC analysis.

In this work, the fabrication of highly dense and single phase $(\text{Hf}_{0.5}\text{Zr}_{0.5})\text{B}_2$ solid solution is accomplished for the first time according to SHS-SPS technique. To date, such two steps route, consisting in the fast preparation of diboride powders by Self-propagating High temperature Synthesis (SHS) followed by their consolidation via SPS, allowed for the obtainment of various standard metal diborides, such as HfB_2 [17], ZrB_2 [18], TaB_2 [18], and TiB_2 [19]. More recently, the same approach was successfully used also for the production of three bulk high entropy diborides (HEBs), namely $(\text{Hf}_{0.2}\text{Mo}_{0.2}\text{Ta}_{0.2}\text{Nb}_{0.2}\text{Ti}_{0.2})\text{B}_2$ [20–22], $(\text{Hf}_{0.2}\text{Mo}_{0.2}\text{Ta}_{0.2}\text{Zr}_{0.2}\text{Ti}_{0.2})\text{B}_2$ [21,22], and $(\text{Hf}_{0.2}\text{Zr}_{0.2}\text{Nb}_{0.2}\text{Mo}_{0.2}\text{Ti}_{0.2})\text{B}_2$ [22]. It should be noted that, when considering standard metal borides, the desired phase can be readily obtained after the first (SHS) step [17–19]. In contrast, when the synthesis of quinary diborides was accomplished with the same technique, multiphasic products were formed, with the desired HEB obtained only after the SPS process [20–22]. Therefore, the latter should be then regarded as a reactive sintering route rather than merely a powder consolidation process. The beneficial role played by graphite when added to SHS powders to improve their densification and promote the formation of a single-phase product, was also evidenced [21,23]. The optimized samples were found to show similar, in some cases superior, mechanical properties, with respect to ceramics with the same nominal composition prepared using alternative methods [22].

In spite of their potential applications, $(\text{Hf}_x\text{Zr}_{1-x})\text{B}_2$ bulk products have been characterized only from the corrosion [12,13], electrocatalytic [13], thermal conductivity [11], and thermal oxidation [7] points of view. On the other hand, a more complete evaluation of their properties is essential to define their potential utilization in different fields, for instance as solar energy absorbers. Indeed, in this context, ZrB_2 - and HfB_2 -based ceramics have been already widely investigated [3,4,24] as they are well known to display spectral selectivity.

A recent paper also reports on the optical properties of $(\text{Hf}_{0.2}\text{Zr}_{0.2}\text{Ta}_{0.2}\text{Mo}_{0.2}\text{Ti}_{0.2})\text{B}_2$ and $(\text{Hf}_{0.2}\text{Nb}_{0.2}\text{Ta}_{0.2}\text{Mo}_{0.2}\text{Ti}_{0.2})\text{B}_2$ to assess the possible utilization of this novel class of solid solutions in the thermal solar energy field [25].

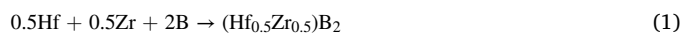
The scope of the present work is twofold. The first one is related to the fabrication of highly dense $(\text{Hf}_{0.5}\text{Zr}_{0.5})\text{B}_2$ samples by the SHS-SPS route, which has not been addressed in the literature so far. Moreover, the optical properties of the resulting ceramics are measured for the first

time, and the influence of surface texture modification was also evaluated. The comparison of the optical behavior of the binary system here obtained with those of monolithic HfB_2 and ZrB_2 is also discussed.

2. Materials and methods

2.1. Synthesis and sintering of $(\text{Hf,Zr})\text{B}_2$ solid solutions

The synthesis of $(\text{Hf}_{0.5}\text{Zr}_{0.5})\text{B}_2$ was performed by SHS using hafnium (Alfa Aesar, cod. 00337, 99.6% pure, <44 μm), zirconium (Alfa Aesar, cod 00847, APS 2–3 μm), and amorphous boron (Sigma-Aldrich, cod 15,580, $\geq 99\%$ pure) powders, according to the reaction stoichiometry:



An excess of boron (10 mol.%), with respect to the stoichiometry value, was used to balance the loss of this reactant by volatilization during the synthesis process and the amount of it consumed for the borothermal reduction of oxides present in metal powders surface. The mixture of SHS precursors was uniaxially cold-pressed and the obtained cylindrical pellets reacted inside a stainless-steel chamber filled with Argon. Once locally initiated by an electrically heated W filament, the synthesis process proceeded in few seconds to provide a porous reacted sample. The latter is then treated for 60 min by ball milling (SPEX CertiPrep, USA, ball to powder weight ratio of 2 with hardened steel milling media) without or in presence of graphite (Sigma-Aldrich, cod 282,863, <20 μm). As explained elsewhere [21], this additive is found to play a crucial role for the elimination of residual oxide impurities present in boride powders and markedly improved their consolidation. On the other hand, residual amounts of graphite could make resistance to oxidation of the ceramic worse. According to previous findings [21], the additive content used in this work is 1 wt%.

Laser light scattering analysis (CILAS 1180, France) was used to determine particle size of the 1 h milled SHS product.

Approximately 22 g of the obtained powders were processed by SPS (515 S model equipment, Fuji Electronic Industrial Co., Ltd., Kanagawa, Japan) under vacuum conditions. Experiments were carried out under temperature-controlled mode, using an infrared pyrometer (CHINO, mod. IR-AHS2, Japan) focused on the external surface of a cylindrical graphite die (AT101, ATAL Srl, Italy; 35 mm external diameter; 18 mm internal diameter; 40 mm height). The following operating conditions were set during SPS runs: 1850 °C or 1950 °C dwell temperature (T_D), for the cases of graphite containing or additive free mixtures, respectively, 200 °C/min heating rate, 20 MPa mechanical pressure, 20 min holding time, 50 °C/min cooling rate down to 650 °C, followed by a natural cooling step. To facilitate samples' release after sintering, their surface was coated with a 0.13 mm thick graphite foil (Alfa Aesar, Karlsruhe, Germany, 99.8 % pure). The use of a graphite felt layer surrounding the die was aimed to limit heat losses by radiation. Cylindrical samples of about 18 mm diameter and about 6 mm height were obtained after SPS.

2.2. Density and thermo-gravimetric analysis

The bulk density of sintered samples was measured by the Archimedes' method using distilled water as immersion medium. Relative density was calculated using the theoretical value of 8.59 g/cm³, based on Rietveld analysis results. The amount of graphite (2.26 g/cm³ density) initially added to the SHS powders was properly considered for determining the theoretical density value for the additive containing samples, as described elsewhere [21].

The oxidation resistance of the $(\text{Hf}_{0.5}\text{Zr}_{0.5})\text{B}_2$ ceramic was evaluated by thermogravimetric analysis (NETZSCH, STA 409 PC Luxx Simultaneous DTA-TGA Instrument, Germany) under 0.1 L/min air flow. To this, non-isothermal (dynamic) tests, consisting of slowly heating (2 °C/min) the sample from room temperature to 1450 °C, have been

performed. The obtained findings are compared with literature data related to DTA-TGA experiments conducted under the same conditions on individual diborides with similar relative densities, namely ZrB_2 , prepared according to the SHS-SPS route [18], and HfB_2 , produced by reactive SPS [26].

2.3. Microstructure and topological characterization

Compositional and microstructural characteristics of SHS powders and SPS products were first assessed by X-Ray Diffraction (XRD) analysis using a SMARTLAB diffractometer with a rotating anode source of copper ($\lambda_{\text{Cu K}\alpha} = 1.54178 \text{ \AA}$) working at 40 kV and 100 mA over a range of scattering angles 2θ from 20° to 80° , in steps of 0.05° with 15 s acquisition time per angle step. The instrument is equipped with a graphite monochromator and a scintillation tube in the diffracted beam. Quantitative analysis of the crystalline phases and structure determinations were performed with the MAUD software (Materials Analysis Using Diffraction), a Rietveld extended program [27].

The cylindrical sintered specimens were sectioned at half height to obtain two portions of 1.8 cm diameter and 2.5 mm thickness. The resulting surfaces were polished with abrasive papers of decreasing grain size and diamond suspensions down to $1 \mu\text{m}$. To evaluate the effect of changes in surface texture on optical properties, chemical attack was applied to half of the polished samples.

Based on previous work [24], chemical etching was performed as follows. An etching solution containing 13 wt % of a 70 % aqueous solution of HNO_3 and 77 wt % of a 40 % aqueous solution of HF was prepared; then the polished surface of the samples was immersed in this solution for 15 s and then rinsed with deionized water.

Microstructural and surface morphology characterization was performed by a scanning electron microscope (SEM, Zeiss EVO MA15, Zeiss, Oberkochen, Germany) equipped with an energy dispersive detector (Xmax 50 Oxford Instruments). SEM micrographs were processed by using an image analysis software (Image-Pro Plus® version 6, Media Cybernetics, Silver Springs, MD, USA) to obtain a quantitative evaluation of microstructural parameters.

Surface texture analysis was performed with a noncontact optical profilometer (Taylor-Hobson CCI MP, Leicester, UK) equipped with a green light and a 20X magnification objective lens.

Four distinct areas were analysed for each sample, and the collected surface data were processed with the Talymap 6.2 software (Taylor-Hobson, Leicester, UK) to obtain 3D areal field parameters.

The 3D texture parameters were evaluated on primary surfaces after denoising (median filter 5×5) and form removing (S–F surface).

2.4. Optical properties

Hemispherical reflectance spectra were acquired at room temperature using a double-beam spectrophotometer (Lambda900 by PerkinElmer) with Spectralon®-coated integration sphere for the $0.25 - 2.5 \mu\text{m}$ wavelength region and a Fourier Transform spectrophotometer (FT-IR “Excalibur” by Bio-Rad) with gold-coated integrating sphere and liquid nitrogen-cooled detector for the range $2.5 - 16.0 \mu\text{m}$. From the experimental reflectance data $R^\cap(\lambda)$, the spectral absorbance $\alpha(\lambda)$ or emittance $\varepsilon(\lambda)$ of fully opaque materials, like in our case, can be obtained, as:

$$\alpha(\lambda) = 1 - R^\cap(\lambda) = \varepsilon(\lambda) \quad (2)$$

Then, the solar absorptance α can be calculated according to the relationship:

$$\alpha = \frac{\int_{0.3\mu\text{m}}^{3\mu\text{m}} \alpha(\lambda) \cdot S(\lambda) d\lambda}{\int_{0.3\mu\text{m}}^{3\mu\text{m}} S(\lambda) d\lambda} \quad (3)$$

where $S(\lambda)$ is the sunlight spectral distribution [28]. Similarly, the total hemispherical emittance ε at the temperature T is given by:

$$\varepsilon = \frac{\int_{0.3\mu\text{m}}^{16.0\mu\text{m}} \varepsilon(\lambda) \cdot B(\lambda, T) d\lambda}{\int_{0.3\mu\text{m}}^{16.0\mu\text{m}} B(\lambda, T) d\lambda} \quad (4)$$

where $B(\lambda, T)$ is the spectral radiance of a blackbody at the temperature T .

3. Results and discussion

3.1. Synthesis and sintering

The high standard reaction enthalpies for the formation of individual hafnium and zirconium diborides from their elements, i.e. $(-\Delta H_f^\circ) = 335.975$ and 322.586 kJ/mol [29], respectively, are responsible for the self-propagating character displayed by their synthesis processes [18, 26]. The same behavior was also experimentally observed in this work during the preparation of the $(\text{Hf}_{0.5}\text{Zr}_{0.5})\text{B}_2$ solid solution according to Eq. (1), with the synthesis reaction which propagated spontaneously and rapidly across the mixture, after local ignition. This is also consistent with the correspondingly high adiabatic temperature ($T_{\text{ad}} = 3203 \text{ K}$) [10], i.e., the maximum temperature achievable in case the SHS process evolves in an isolated system, which is well above of the empirical threshold limit of 1800 K [30]. For the same system, the combustion synthesis event was also observed to occur when Zr, Hf, and B powders (1:1:4 at. ratio) were mechanically treated for 24 min in a planetary ball milled using a ball to powder weight ratio equal to 17.35 [10].

The conversion of raw reactants into the desired phase was checked by XRD analysis. Results are shown in Fig. 1a with the corresponding amounts of the detected phases reported in Supplementary Table S1 along with the microstructural parameters obtained by the Rietveld method.

While the SHS process of individual metal diborides led to ZrB_2 [18], and HfB_2 [26] powders with neither residual reactants nor secondary phases, a multiphasic product is obtained when considering the binary system. Quantitative analysis reveals that the content (in percentage by weight) of the $(\text{Hf}_{0.5}\text{Zr}_{0.5})\text{B}_2$ phase is 21%, with HfB_2 , ZrB_2 , and Zr also found in the powders, i.e. 31.2, 43.0, and 4.5 %, respectively. Minor amounts of other secondary phases, in particular metal oxides (ZrO_2 and HfO_2), are also likely present, even though they were not clearly detectable by this analysis. The low conversion degree of initial reactants into the desired phase could be attributed to the extreme conditions involved during SHS, with Zr and Hf elements not allowed to uniformly diffuse across the sample during the very rapid occurrence of the synthesis process.

The particle size parameters determined for the SHS powders ball milled for 1 h are $d_{10} = 0.18 \pm 0.03 \mu\text{m}$, $d_{50} = 1.1 \pm 0.1 \mu\text{m}$, $d_{90} = 7.3 \pm 0.3 \mu\text{m}$, and $d_{43} = 2.6 \pm 0.1 \mu\text{m}$.

These powders were sintered by SPS either additive-free or in presence of graphite. The consolidation process of powders with no graphite was conducted at $T_D = 1950^\circ\text{C}$, as for the case of high entropy borides [20], and resulted in 94.2% dense samples (8.09 g/cm^3 absolute density). The corresponding XRD pattern is shown in Fig. 1b, while the

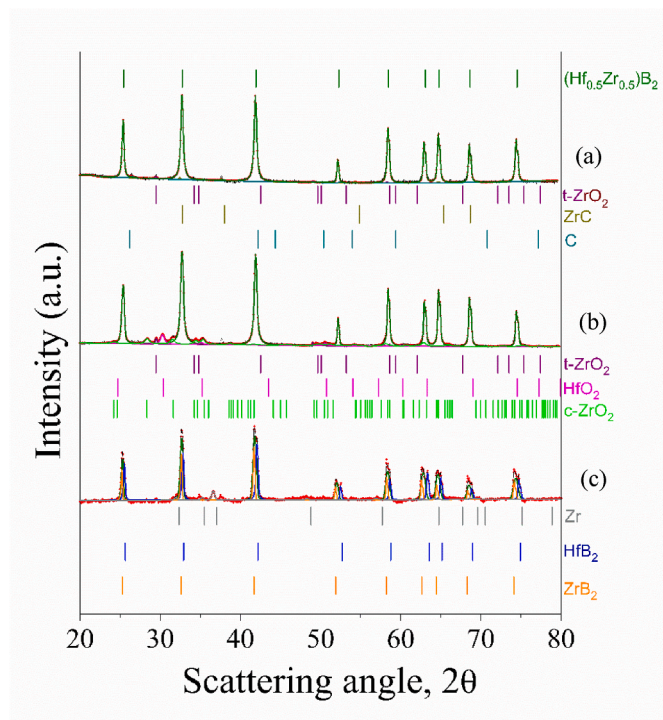


Fig. 1. XRD patterns of SHS (a), and SPS products with no additive at $T_D = 1950^\circ\text{C}$ (b) and in presence of 1 wt% graphite at $T_D = 1850^\circ\text{C}$ (c). Red dots are experimental data, the continuous lines are the calculated best fit.

related phases' amount and microstructure parameters are listed in Table S2. It is apparent that the yield in the desired binary phase is highly improved, from 21 to 85.5 wt%, after SPS. However, the sintered ceramic is rich of oxides, namely ZrO_2 (tetragonal and cubic), and HfO_2 , 8.1 and 6.4 wt%, respectively. In the latter regard, Fig. 1c and Table S2 evidence the unequivocal beneficial effect produced by the introduction 1 wt% graphite for the removal of such impurities, which were reduced to 2.1 wt% (ZrO_2), from SHS powders. This fact concurrently determined a further raise of sample consolidation, with the obtainment of relative densities of about 98.3 % (8.21 g/cm³ absolute density) at lower dwell temperatures with respect to the case of additive-free powders, 1850 instead of 1950 °C, respectively.

As observed elsewhere for the case of high-entropy systems [23], the obtainment of highly pure boride ceramics at relatively milder processing conditions is a direct consequence of the removal of surface oxides from powder particles, which makes them more reactive, so that the synthesis of single-phase products is promoted. Almost fully dense samples consisting of 96.6 wt% of $(\text{Hf}_{0.5}\text{Zr}_{0.5})\text{B}_2$, with traces of ZrC (0.6 wt%) and residual graphite (0.7 wt%), other than minor amounts of oxides, are finally obtained. The latter ceramic is subjected to further characterization, as discussed in what follows.

3.2. TGA test

The oxidation behavior of the dense binary diboride sample produced at 1850 °C with 1 wt%C was examined by conducting dynamic TGA experiments in air flow. Fig. 2 shows the corresponding curve, expressed as normalized weight gain. For the sake of comparison, results relative to monophasic ZrB_2 (98.5% relative density) [18], and HfB_2 (97.6% relative density) [26] samples prepared according the SHS-SPS and R-SPS routes, respectively, are also shown.

Negligible weight changes were observed up to about 800 °C for the three systems. Above such temperature level, TGA curves increase in an exponential way, although with different rates, being the ZrB_2 sample more sensitive to the high-temperature oxidizing environment and HfB_2

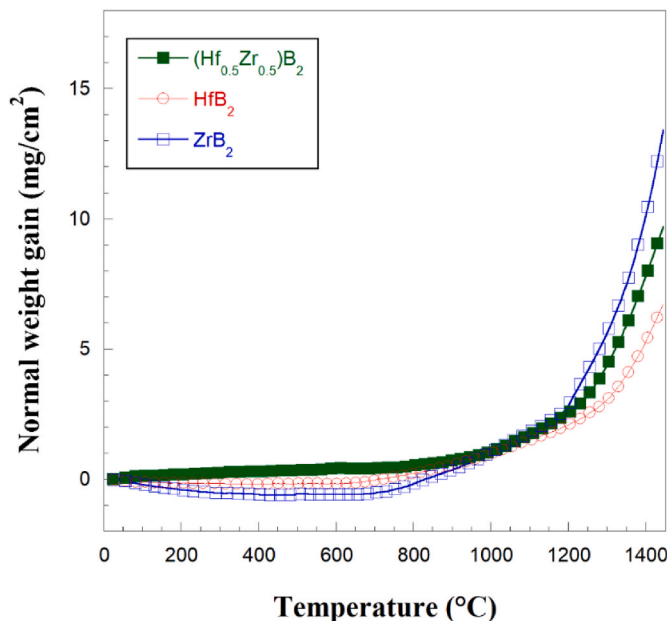


Fig. 2. Comparison of specific weight changes during TGA oxidation test in air of $(\text{Hf}_{0.5}\text{Zr}_{0.5})\text{B}_2$ sample prepared by SPS ($T_D = 1850^\circ\text{C}$, 1 wt%C) in this work as a function of temperature (heating rate equal to $2^\circ\text{C}/\text{min}$). Literature data of individual diborides (HfB_2 , ZrB_2) are also reported for comparison [18,26].

the system which gain less weight, while an intermediate behavior is displayed by the solid solution.

The outcomes obtained in this work are consistent with thermal oxidation resistance data reported in the literature for flash sintered 95% dense $(\text{Hf}_{0.5}\text{Zr}_{0.5})\text{B}_2$ samples tested by TGA-DSC in flowing air [7]. In particular, it was found that no noteworthy weight gain was recorded up to 800 °C. However, as a difference, a weight loss was observed to occur from about 800 to 1000 °C, which was ascribed by the authors to the evaporation of some amorphous phases present in flash-sintered samples [7].

Based on the results above, it is possible to state that the $(\text{Hf}_{0.5}\text{Zr}_{0.5})\text{B}_2$ system shows a good resistance to oxidation up to 800 °C, whereas, as for the case of standard Zr- and Hf-diborides, suitable additives such as Si-containing compounds (SiC , MoSi_2 , HfSi_2 , etc.), should be introduced if the ceramic has to be exposed to more severe temperature and oxidizing environments [17,26,31,32].

3.3. Microstructure and topological characteristics

Both the polished and the etched samples were analysed by SEM/EDS to characterize their microstructure, and to correlate surface texture features to the optical properties.

The microstructure of the polished sample obtained with the addition of 1 wt% carbon (relative density 98%) is shown in Fig. 3, where the surface is revealed by secondary and backscattered electrons. Residual porosity, closed and rounded, with an average size of 0.64 μm , is uniformly distributed and mainly incorporated into the grains of the binary phase. The densification process induced a grain growth, thus reaching an average size of about 11 μm .

Backscattered electron images show a phase contrast effect, essentially crystallographic, due to electron channelling phenomena linked to the different grains' orientations. After densification, the material reached an excellent homogeneity, with the percentage of binary phase in the ceramic above 96%. This suggests that, during the SPS process, the interdiffusion of metallic elements was rapid and allowed to minimize segregation and avoid core-shell phenomena.

Fig. 4 shows a SEM micrograph of the sample surface, together with the corresponding EDX maps. The element distribution maps confirm

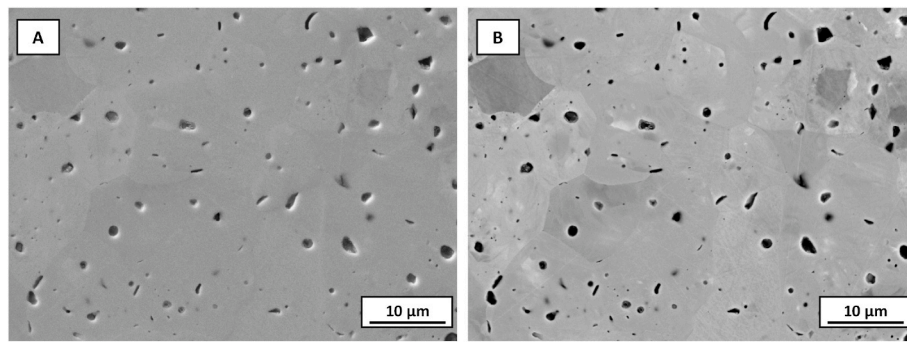


Fig. 3. SEM micrographs of the $(\text{Hf}_{0.5}\text{Zr}_{0.5})\text{B}_2$ sample produced by SPS (1850 °C) from SHS powders in presence of 1 wt% graphite: A) Secondary and B) back-scattered electron images.

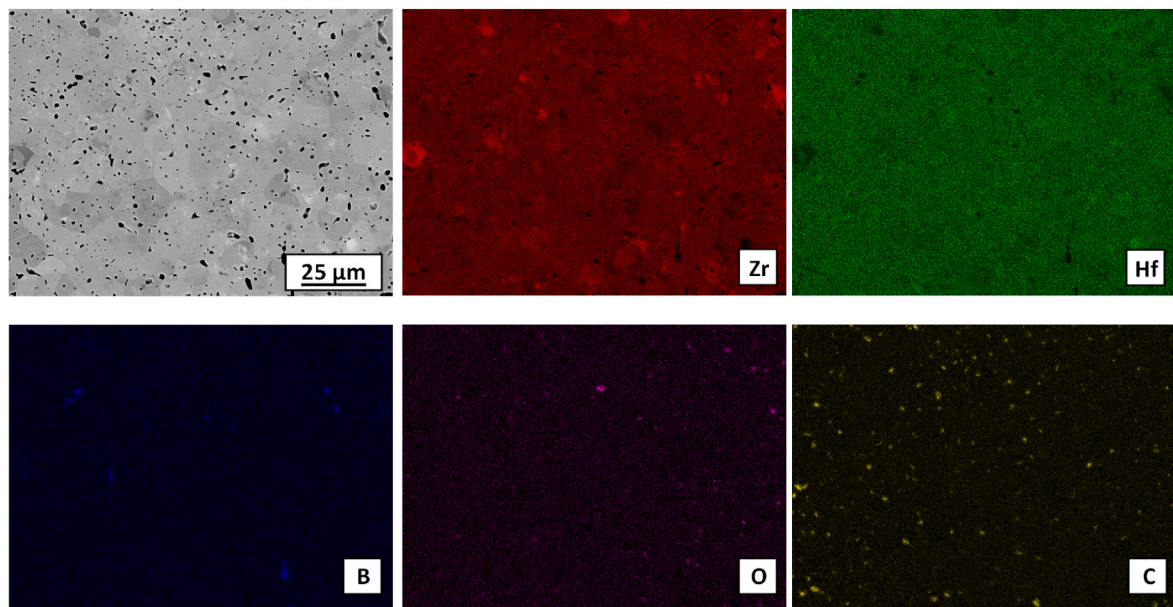


Fig. 4. SEM micrograph and related EDX elemental maps collected on $(\text{Hf}_{0.5}\text{Zr}_{0.5})\text{B}_2$ sample produced by SPS (1850 °C) from SHS powders in presence of 1 wt % graphite.

the previous observations. The sample is rather homogeneous in composition: in particular, the metallic elements, Hf and Zr, are uniformly distributed over the whole analysed surface. In accordance with the Rietveld analysis (Table S2), residual carbon and some remaining oxides are also observed locally.

To increase the absorption of solar radiation, the surface texture was modified by means of chemical etching. Figs. 5 and 6 show the surface of the sintered sample (1 wt%C) after chemical attack.

The etching solution consists of nitric acid and hydrofluoric acid. Nitric acid is a powerful oxidant and acts by oxidizing the metal cations and the boride ion forming tetravalent cations and soluble borates. However, when used alone, HNO_3 does not provide any etching effect, as it instead reinforces the passive film, naturally formed in the air, mainly consisting of mixed hafnium and zirconium oxides that protect the surface of the ceramic material.

Hydrofluoric acid has the double function of breaking the passive

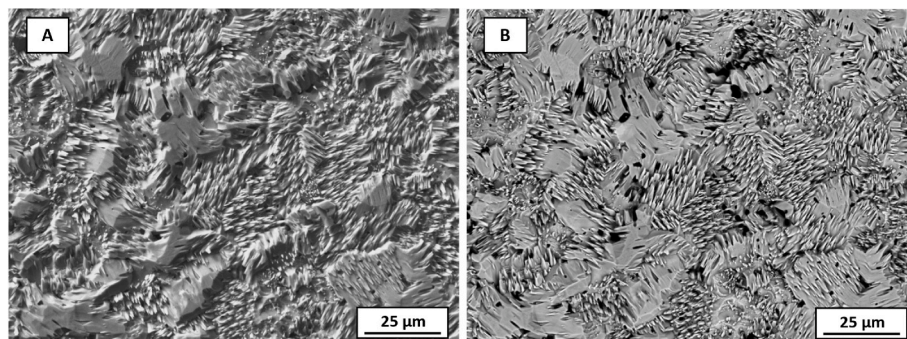


Fig. 5. SEM micrograph of the etched sample. A) Secondary and B) backscattered electron images.

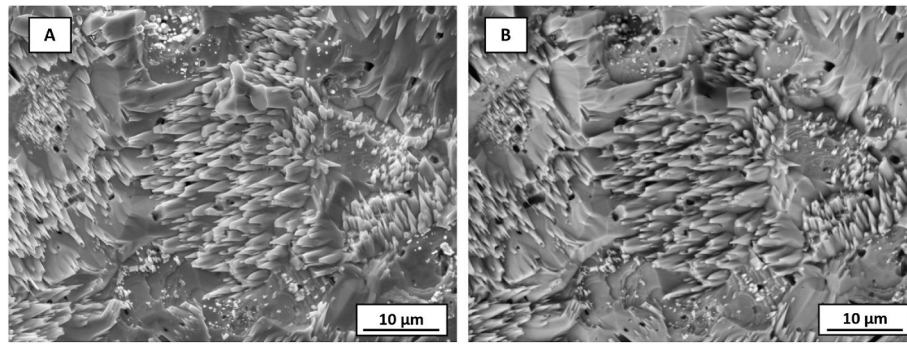


Fig. 6. SEM micrograph of the etched sample, details of etched morphology at higher magnification. A) Secondary and B) backscattered electron images.

film, allowing substrate oxidation, and complexing the metal cations, thus preventing their precipitation as insoluble fluorides, if the concentration of fluoride ions is sufficiently high.

As suggested by XRD analysis data reported in [Supplementary Fig. S1](#), the etching process does not generate any new phases, while it induced a rather uniform dissolution of the elements in the solid solution. Nonetheless, it significantly changed the surface morphology, which became very irregular, thus revealing different morphological characteristics.

The attack was preferentially localized on certain grains: in these areas the binary phase was strongly attacked, and an acicular morphology was obtained. On the other hand, other areas appeared only slightly attacked and retained a flat morphology. In addition, in some strongly etched areas, the attack occurred in a generalized manner, thus forming flat regions without texturing.

The evaluation of the surface extension of these areas was carried out by image analysis. It was found that the strongly textured portion covers about 62% of the entire surface, while the slightly attacked and the flat areas at the base account for 18 and 20%, respectively.

Details of the etched surface can be deduced from [Fig. 7a](#) and [7b](#), where two micrographs obtained from the cross-sectional observation are shown. The etched areas are characterized by the presence of variably oriented truncated pinnacles, with an average height of 2 µm, and spaced about 600 nm apart.

The EDX maps collected on the etched sample are reported in [Fig. 8](#). The binary phase appears to be uniformly attacked, with no evidence of preferential dissolution of elements present in the solid solution. In fact, a rather homogeneous distribution of the main elemental constituents was observed over the entire surface, with the presence of residual carbon which was apparently not dissolved by the mixture of mineral acids.

[Fig. 9](#) shows a 3D map of the etched surface ([Fig. 9a](#)) and the average values of the height parameters together with the relative uncertainties collected on both unetched (polished) and etched samples ([Fig. 9b](#)). The

unetched surface shows typical values of polished surfaces, with Sa and Sq values close to 79 and 101 nm, respectively; the surface displays a slight prevalence of smooth irregularities (shallow peaks max 0.5–0.6 nm) and the height values are quite symmetrically dispersed with respect to the mean plane, following an essentially Gaussian distribution ($Ssk \approx 3$). The chemical treatment substantially modifies the texture, thus producing a much more irregular surface, with a slight predominance of valleys/depression (negative value of Ssk) characterized by Sq and Sa values of one order of magnitude higher than the unetched surface. The analysis of the profiles extracted from the studied surfaces shows that the chemical attack proceeded by eroding the initial sample by about 2.2 µm.

3.4. Optical properties

[Fig. 10](#) shows the hemispherical reflectance spectra of polished and etched sample, together with those of pure polished ZrB_2 [3] and HfB_2 [4], for comparison. It is interesting to notice that the curve of the pristine binary boride shows a different spectral shape with respect to the individual ZrB_2 and HfB_2 , as expected from the formation of the solid solution, which is a new material rather than the simple mix of two components. We can see that the spectrum of $(Hf_{0.5}Zr_{0.5})B_2$ from time to time coincides with that of ZrB_2 or HfB_2 (see [Fig. 10a](#) for the range 0.3–16.0 µm and [Fig. 10b](#) for shorter infrared wavelengths), while it is differentiated from them in the ranges ~0.9–1.9 µm and ~3.5–5.7 µm, respectively. In these regions, the binary sample shows either a slightly higher reflectance than both ZrB_2/HfB_2 (in the first interval), or intermediate characteristics between them (in the second one).

When the effect of the etching process on optical properties is concerned, it is possible to clearly appreciate the dramatic decrease of the reflectance in the etched surface with respect to the pristine one, across the whole investigated range. The reflectance decrease is wavelength-dependent. If we consider the ratio R_{e-p} between the spectra of etched and pristine sample, its value is the lowest in the range ~1.3–2.0 µm

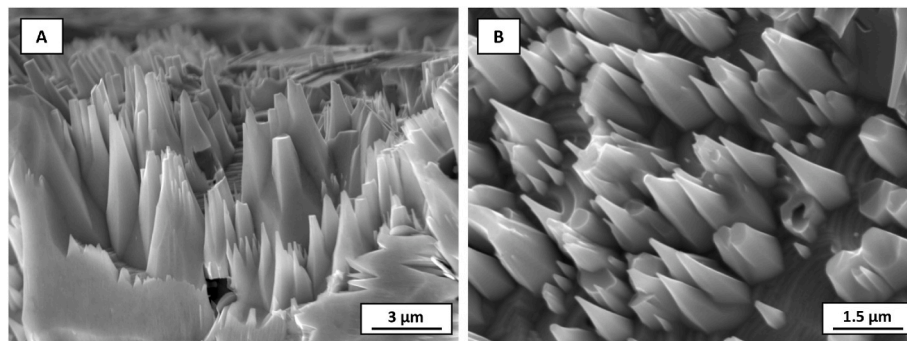


Fig. 7. SEM micrograph of the etched sample, with details of etched morphology at higher magnification. A) SE image obtained from cross-section observation; B) SE image of textured areas.

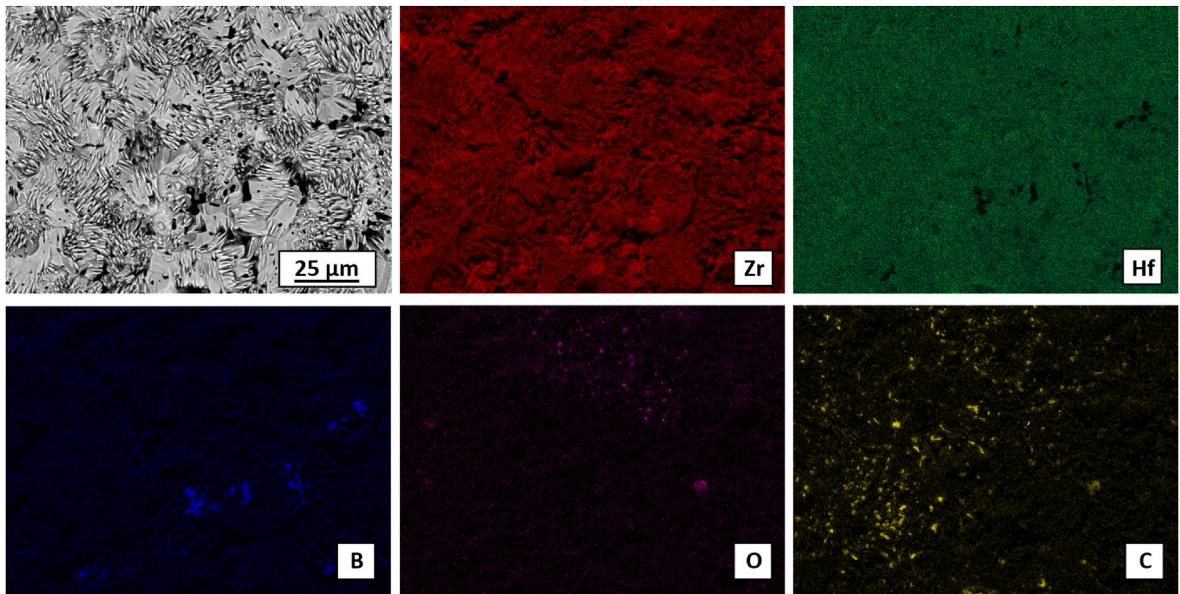


Fig. 8. SEM micrograph and related EDX elemental maps collected on an etched sample.

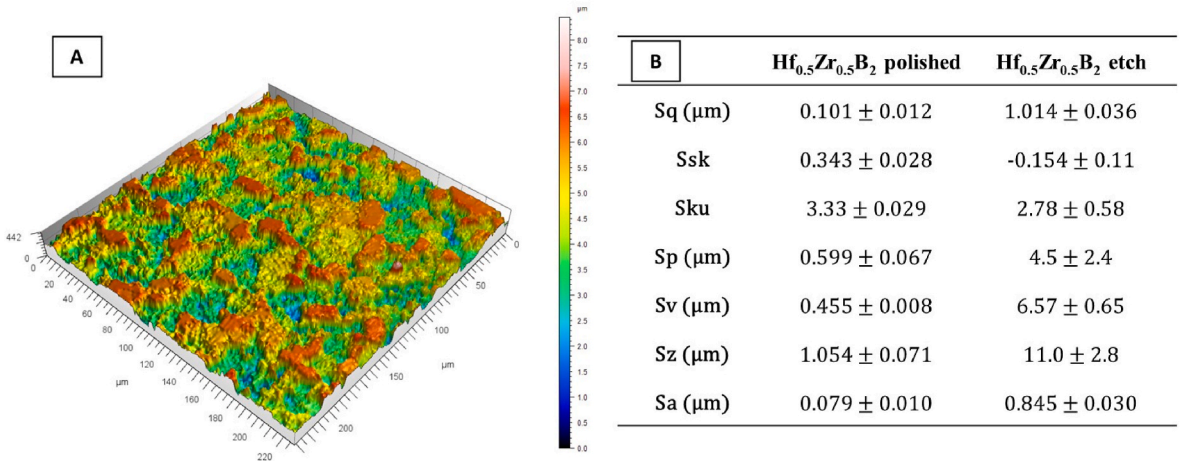


Fig. 9. (a) Areal surface maps of etched surface; (b) Height parameter values evaluated on polished and etched samples.

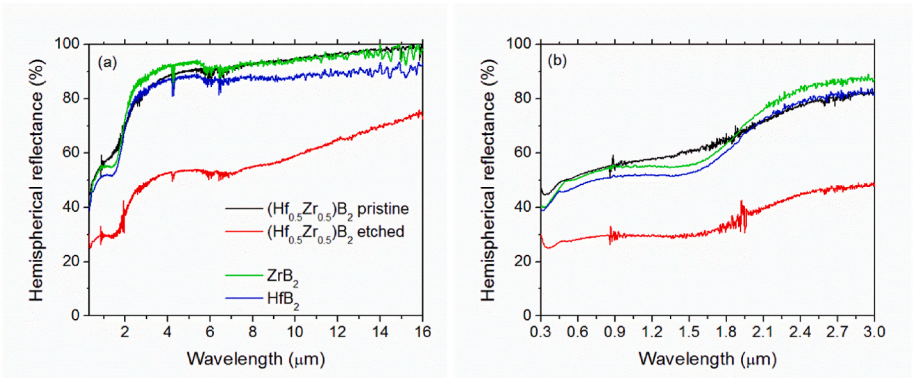


Fig. 10. Hemispherical reflectance spectra of pristine and etched binary borides, and single Zr- and Hf borides, for reference. (a) Full range 0.3–16.0 μm and (b) solar spectrum range 0.3–3.0 μm.

wavelengths ($R_{e-p} = 0.47 \div 0.55$), with an absolute minimum value around 1.5 μm; it shows a secondary minimum around 7 μm (0.57), with values between 0.60 and 0.57 in the range ~2–7 μm and finally

monotonically increases from 0.57 to 0.76 for wavelengths above ~7 μm.

Following the approach shown in Refs. [33,34], the obtained result

on optical properties can be qualitatively explained in terms of the structures created by the etching treatment and their sizes. The involved light-material interaction phenomena are light trapping (when the radiation wavelength is similar to the size of surface features) and increase the effective surface (when the surface features are much larger than radiation wavelength). On the other hand, when the surface features are smaller than the wavelength of the involved radiation, we expect an increasingly reduced effect. In our case, the pointy pyramids created by the etching process appear not homogeneous in orientation, size and density on the specimen surface, likely because of the non-homogenous etching rate on the differently-oriented crystal grains, as noted above. Therefore, a quantitative assessment of the size distribution of etching-produced pinnacles from SEM images is difficult. However, we can make some qualitative comments: the height and spacing of the pinnacles agrees with trapping effects of radiation wavelengths shorter than about 2 μm , corresponding to the spectral range of the observed maximum reduction of the reflectance (i.e. maximum increase of absorbance or emittance), while the presence of the relatively few depressed large flat areas, whose typical sizes are smaller than 10 μm , explains the (lower) reduction of reflectance (i.e. the lower increase of absorbance or emittance) at the corresponding wavelengths and is consistent with the cutoff behavior around 7 μm observed in the reflectance ratio R_{e-p} . In other words, the radiation with wavelengths shorter than the cutoff experiences, depending on its specific wavelength, the increase of the effective surface available for interaction and/or the trapping within surface features. Thus, both these effects contribute to the observed decrease of reflectance at these wavelengths. On the contrary, longer-wavelength radiation cannot be trapped and does not see any surface increase, so that the reflectance tends to recover the value of the original surface.

For the sake of comparison, Fig. 11 shows the spectra of the solid solutions and those of two materials commercially available and used in solar power plants: SiC [35] and Al_2O_3 [36]. SiC is characterized by the lowest reflectance in the spectral range of solar radiation, but also in the remaining of the infrared range, which entails high thermal emittance. Al_2O_3 has very poor solar absorption properties (see the high reflectance in Fig. 11b), and a high thermal emittance as well.

Fig. 12 shows the temperature-dependent values of thermal emittance ϵ and spectral selectivity α/ϵ of the binary samples, the reference single borides and the two commercial reference materials SiC and Al_2O_3 [38]. As for emittance, the pristine binary boride shows intermediate values between the single borides, and a solar absorptance slightly lower than ZrB_2 , while the etched binary sample is characterized by significantly increased solar absorptance and thermal emittance. The emittance of both binary samples is considerably lower than that of SiC at all temperatures including the highest one here considered ($\epsilon = 0.57$ and 0.25 at $T = 1700$ K for the etched and pristine binary pellets, respectively, to be compared to $\epsilon = 0.83$ for SiC at the same

temperature). If the spectral selectivity is concerned, again the pristine sample shows an intermediate behavior between the single borides, and a curve superimposed to that of HfB_2 for temperatures >1100 K. Interestingly, the etched sample keeps the spectral selectivity, even if with lower values. This favorably compares the binary samples to both SiC and Al_2O_3 , none of which can be considered spectrally selective. Finally, if we compare the pristine binary boride with other kinds of advanced ceramics, for instance MAX phases, the values of the optical parameters appear fully comparable [39].

From the α and ϵ parameters, it is possible to evaluate the opto-thermal conversion efficiency of the solar absorber, defined as [34]:

$$\eta_{o-th}(T) = \alpha - \epsilon \cdot \frac{\sigma \cdot T^4}{C \cdot I_{\text{solar}}} \quad (5)$$

where $\sigma = 5.67 \times 10^{-8} \text{ W}/(\text{m}^2 \text{ K}^4)$ is the Stefan-Boltzmann constant, T is the absorber temperature, C the solar concentration ratio of the solar plant where the absorber is used (i.e. the ratio between the overall area of solar-collecting surfaces in the plant –mirrors or lenses– and the area of the solar absorbing surface) and $I_{\text{solar}} = 1 \text{ kW}/\text{m}^2$ is the standard solar radiation intensity at 1 sun.

Fig. 13a compares the opto-thermal efficiency of samples as a function of temperature for four values of the solar concentration ratio $C = 100$ and 300 (compatible with solar tower systems), $C = 1000$ (solar towers or solar dishes) and $C = 3000$ (solar dishes) [40]. It is immediate to see the significant improvement in efficiency obtained with the etching treatment, especially at high concentration ratios. For mid concentration ratios, the etched sample is better performing for $T \leq 1600$ K ($C = 500$) and $T \leq 1400$ K ($C = 300$), while, for higher temperatures, the choice of the untreated pristine sample should be privileged at these concentration ratios, because of its lower emittance. Fig. 13b compares the opto-thermal efficiency of the etched binary boride to the performances of the two commercial reference materials, showing that it is always much more efficient than Al_2O_3 . In addition, in the investigated space of parameters, remarkably, it is also better than SiC at high temperatures and moderate values of concentration ratio ($T \geq 1300$ K or 1500 K for $C = 300$ or 500, respectively). At $T = 1700$ K and $C = 1000$, the binary boride has the same efficiency than SiC, and a higher one at higher temperatures (not shown in Figure).

4. Conclusions

The $(\text{Hf}_{0.5}\text{Zr}_{0.5})\text{B}_2$ solid solution was produced in highly dense form by the SHS-SPS processing route, and the optical properties of the resulting ceramic were evaluated for the first time. Based on the obtained results, it is possible to draw the following conclusions.

- 1) The individual diborides are main phases, i.e. ZrB_2 (43 wt%) and HfB_2 (31 wt%), present in the SHS product which contains only 21 wt

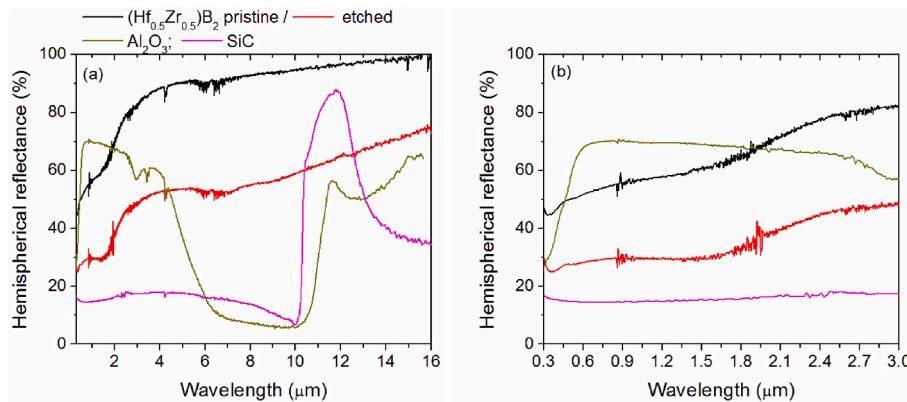


Fig. 11. Comparison of the spectra of solid solutions and Al_2O_3 and SiC [37].

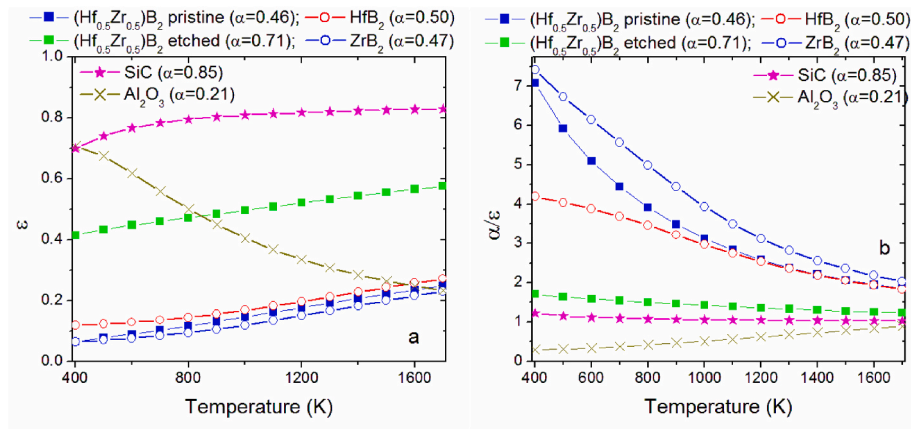


Fig. 12. Comparison of the calculated temperature-dependent (a) thermal emittance ϵ , and (b) spectral selectivity (α/ϵ). The solar absorptance values are indicated in the legend. SiC and Al_2O_3 data are taken from [38].

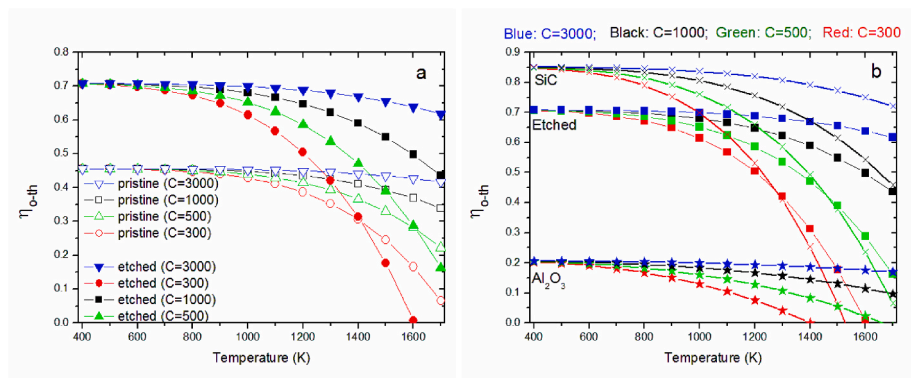


Fig. 13. Opto-thermal efficiency as a function of the temperature. (a) Comparison of the two binary borides. Hollow symbols: untreated sample. Filled symbols: etched sample. (b) Comparison of the etched binary sample to two commercial reference materials (SiC and Al_2O_3). Meaning of symbols: crosses: SiC; filled squares: etched binary boride; stars: Al_2O_3 . The color code is referred to the values of the solar concentration ratio, as explained in legend.

% of the desired binary compound. On the other hand, the yield in the $(\text{Hf}_{0.5}\text{Zr}_{0.5})\text{B}_2$ phase increased to 85 wt%, when the SHS powders were consolidated at 1950 °C by SPS, which should be then considered as a reactive sintering process. As a drawback, the resulting ceramics were rich of oxide impurities, whose presence does not permit to obtain fully dense samples.

- 2) The introduction of 1 wt% of graphite markedly purifies the sintered product, with a decrease of the oxide content (from 14.5 to 2.1 wt%) by carbothermal reduction mechanism; in parallel, powder densification is promoted, with an increase in the relative density from about 94% to values exceeding 98%. Moreover, the removal of surface oxides by graphite made powders more reactive, so that the obtainment of a single-phase product by SPS was achieved at lower temperature, i.e. 1850 instead of 1950 °C.
- 3) The $(\text{Hf}_{0.5}\text{Zr}_{0.5})\text{B}_2$ system was found to be thermally stable in air up to 800 °C, similarly to the individual diborides, therefore, with reference to the solar absorber application, no oxidation issues are expected below this temperature. At higher temperatures, again similarly to the individual borides, they can be used either in vacuum or under inert atmosphere, or, in case of planned use under oxidizing environments, the introduction of suitable silicon-containing additives (SiC, MoSi₂, etc) in the ceramics should be considered.
- 4) Chemical etching modified the surface of the binary boride, producing a surface with high roughness characterised by the presence of pinnacle structures of the order of 0.4–2 μm size and few large, heavily attacked, flat areas of typical size below 10 μm .

Texturisation significantly modifies the optical properties of the material due to the different interaction of the various spectral components of sunlight and thermal radiation with surface textures of different sizes. In particular, the optical parameters are modified as follows: the solar absorptance α is increased, the spectral selectivity α/ϵ is decreased, but still maintained ($\alpha/\epsilon > 1$). Consequently, the opto-thermal efficiency of the etched sample is significantly increased at all the investigated temperatures if the material is used in a system with solar concentration ratios $C = 1000 \div 3000$ and at temperatures $T < 1400 \div 1600$ K for $C < 1000$. For those concentration ratios and higher operating temperatures, the unetched sample should be privileged. The considered materials, in particular the etched one, favorably compares to the existing commercial materials used in solar absorbers.

The fabrication route proposed in this work, also employed successfully for the obtainment of bulk single-phase high-entropy borides, is intended to be valid also when considering additional multicomponent boride systems (binary, ternary, etc.).

CRedit authorship contribution statement

Simone Barbarossa: Writing – review & editing, Investigation. **Antonio M. Locci:** Writing – review & editing. **Giacomo Cao:** Writing – review & editing, Validation. **Sebastiano Garroni:** Writing – review & editing, Investigation. **Andrea Balbo:** Writing – review & editing, Validation, Supervision, Methodology, Investigation. **Federica Zanutto:** Investigation. **Elisa Sani:** Writing – original draft, Validation, Supervision, Methodology, Investigation. **Roberto Orrù:** Writing –

original draft, Validation, Supervision, Methodology.

Declaration of competing interest

The authors declare that they have no known competing financial interests or personal relationships that could have appeared to influence the work reported in this paper.

Data availability

Data will be made available on request.

Acknowledgements

One of the authors (S.B.) performed his activity in the framework of the International Ph.D. in Innovation Sciences and Technologies at the University of Cagliari, Italy. This work has been developed within the framework of the project eINS- Ecosystem of Innovation for Next Generation Sardinia (cod. ECS 00000038) funded by the Italian Ministry for Research and Education (MUR) under the National Recovery and Resilience Plan (PNRR) - MISSION 4 COMPONENT 2, "From research to business" INVESTMENT 1.5, "Creation and strengthening of Ecosystems of innovation" and construction of "Territorial R&D Leaders". A part of this study has been developed in the framework of the research activities carried out within the Project "Network 4 Energy Sustainable Transition—NEST", Spoke 1, Project code PE0000021, funded under the National Recovery and Resilience Plan (NRRP), Mission 4, Component 2, Investment 1.3— Call for tender No. 1561 of October 11, 2022 of Ministero dell'Università e della Ricerca (MUR); funded by the European Union—NextGenerationEU. This work was also supported by Fondazione di Sardegna (2020) in the framework of the Advanced design of "Thermodynamically-stable Nanocrystalline Alloys (ATHENA)" project, CUP F75F21001370007. Thanks are due to CNR-INO technicians Mr. M. Pucci and Mr. M. D'Uva for technical assistance. The authors acknowledge the GAUSS-CeSAR (Centro Servizi d'Ateneo per la Ricerca) of the University of Sassari for X-ray diffraction analyses.

Appendix A. Supplementary data

Supplementary data to this article can be found online at <https://doi.org/10.1016/j.solmat.2024.112755>.

References

- [1] W.G. Fahrenholtz, G.E. Hilmas, I.G. Talmy, J.A. Zaykoski, Refractory diborides of zirconium and hafnium, *J. Am. Ceram. Soc.* 90 (5) (2007) 1347–1364, <https://doi.org/10.1111/j.1551-2916.2007.01583.x>.
- [2] W.G. Fahrenholtz, G.E. Hilmas, Ultra-high temperature ceramics: materials for extreme environments, *Scripta Mater.* 129 (2017) 94–99, <https://doi.org/10.1016/j.scriptamat.2016.10.018>.
- [3] E. Sani, et al., Optical properties of dense zirconium and tantalum diborides for solar thermal absorbers, *Renew. Energy* 91 (2016), <https://doi.org/10.1016/j.renene.2016.01.068>.
- [4] C. Musa, et al., Optical characterization of hafnium boride and hafnium carbide-based ceramics for solar energy receivers, *Sol. Energy* 169 (2018), <https://doi.org/10.1016/j.solener.2018.04.036>.
- [5] R. Roucka, et al., Epitaxial semimetallic HfZr_{1-x}B₂ templates for optoelectronic integration on silicon, *Appl. Phys. Lett.* 89 (2006) 242110.
- [6] R. Roucka, et al., Structural and optical properties of ZrB₂ and HfZr_{1-x}B₂ films grown by vicinal surface epitaxy on Si(1 1 1) substrates, *Solid State Electron.* 52 (2008) 1687–1690.
- [7] J. Belisario, S. Mondal, I. Khakpour, A. Franco Hernandez, A. Durygin, Z. Cheng, Synthesis and flash sintering of (Hf_{1-x}Zr_x)B₂ solid solution powders, *J. Eur. Ceram. Soc.* 41 (2021) 2215–2225.
- [8] D. Liu, B. Jiao, H. Zhang, S. Zhang, J. Liu, High-aspect-ratio single-crystalline (Hf_xZr_{1-x})B₂ micron-rods: low-temperature, highly-efficient synthesis and oriented growth mechanism, *CrystEngComm* 24 (2022) 4399–4407.
- [9] S. Otani, T. Aizawa, N. Kieda, Solid solution ranges of zirconium diboride with other refractory diborides: HfB₂, TiB₂, TaB₂, NbB₂, VB₂ and CrB₂, *J. Alloys Compd.* 475 (2009) 273–275.
- [10] M.A. Avilés, J.M. Córdoba, M.J. Sayagués, M.D. Alcalá, F.J. Gotor, Mechanochemical synthesis of Hf_{1-x}Zr_xB₂ solid solution and Hf_{1-x}Zr_xB₂/SiC composite powders, *J. Am. Ceram. Soc.* 93 (2010) 696–702.
- [11] D.L. McClane, W.G. Fahrenholtz, G.E. Hilmas, Thermal properties of (Zr,TM)B₂ solid solutions with TM = Hf, Nb, W, Ti, and Y, *J. Am. Ceram. Soc.* 97 (2014) 1552–1558.
- [12] S.J. Sitler, I. Charit, K.S. Raja, Room temperature corrosion behavior of ZrB₂-HfB₂ solid solutions in acidic and basic aqueous environments, *Electrochim. Acta* 246 (2017) 173–189.
- [13] S.J. Sitler, K.S. Raja, I. Charit, ZrB₂-HfB₂ solid solutions as electrode materials for hydrogen reaction in acidic and basic solutions, *Mater. Lett.* 188 (2017) 239–243.
- [14] S.J. Sitler, K.S. Raja, I. Charit, Hot corrosion behavior of ZrB₂-HfB₂ solid solutions in KCl and K₂SO₄ at 1500°C, *Ceram. Int.* 43 (2017) 17071–17085.
- [15] D. Liu, T. Wen, B. Ye, X. Zhou, Y. Chu, Molten salt synthesis, characterization, and formation mechanism of superfine (Hf_xZr_{1-x})B₂ solid-solution powders, *J. Am. Ceram. Soc.* 102 (2019) 3763–3770.
- [16] T. Wen, B. Ye, H. Liu, S. Ning, C.Z. Wang, Y. Chu, Formation criterion for binary metal diboride solid solutions established through combinatorial methods, *J. Am. Ceram. Soc.* 103 (2020) 3338–3348.
- [17] C. Musa, R. Licheri, R. Orrù, G. Cao, Synthesis, sintering, and oxidative behavior of HfB₂-HfSi₂ ceramics, *Ind. Eng. Chem. Res.* 53 (2014) 9101–9108.
- [18] R. Licheri, C. Musa, R. Orrù, G. Cao, D. Sciti, L. Silvestroni, Bulk monolithic zirconium and tantalum diborides by reactive and non-reactive spark plasma sintering, *J. Alloys Compd.* 663 (2016) 351–359.
- [19] E. Sani, M. Meucci, L. Mercatelli, A. Balbo, C. Musa, R. Licheri, R. Orrù, G. Cao, Titanium diboride ceramics for solar thermal absorbers, *Sol. Energy Mater. Sol. Cells* 169 (2017) 313–319.
- [20] G. Tallarita, R. Licheri, S. Garroni, R. Orrù, G. Cao, Novel processing route for the fabrication of bulk high-entropy metal diborides, *Scripta Mater.* 158 (2019) 100–104.
- [21] S. Barbarossa, R. Orrù, S. Garroni, R. Licheri, G. Cao, Ultra high temperature high-entropy borides: effect of graphite addition on oxides removal and densification Behaviour, *Ceram. Int.* 47 (2021) 6220–6231.
- [22] S. Barbarossa, et al., Fabrication and characterization of quinary high entropy-ultra-high temperature diborides, *Ceramics* 4 (2021) 108–120.
- [23] S. Barbarossa, M. Murgia, R. Orrù, and G. Cao, "Processing conditions optimization for the synthesis and consolidation of high-entropy diborides," *Eurasian Chem. J.*, vol. 2021, pp. 213–220, 23AD.
- [24] L. Silvestroni, et al., An overview of ultra-refractory ceramics for thermodynamic solar energy generation at high temperature, *Renew. Energy* 133 (2019) 1257–1267, <https://doi.org/10.1016/j.renene.2018.08.036>.
- [25] S. Barbarossa, R. Orrù, G. Cao, A. Balbo, F. Zanotto, E. Sani, Optical properties of bulk high-entropy diborides for solar energy applications, *J. Alloys Compd.* 935 (2023), 167965.
- [26] C. Musa, R. Orrù, D. Sciti, L. Silvestroni, G. Cao, Synthesis, consolidation and characterization of monolithic and SiC whiskers reinforced HfB₂ ceramics, *J. Eur. Ceram. Soc.* 33 (2013) 603–614.
- [27] L. Lutterotti, R. Ceccato, R. Dal Maschio, E. Paganì, Quantitative analysis of silicate glass in ceramic materials by the Rietveld method, *Mater. Sci. Forum* 278 (1998) 87–92.
- [28] Standard Tables for Reference Solar Spectral Irradiances: Direct Normal and Hemispherical on 37° Tilted Surface, Active Standard ASTM G173. ASTM G173 - 03," 2012.
- [29] I. Barin, Thermochemical Data of Pure Substances, VHC, Weinheim, Germany, 1989.
- [30] Z.A. Munir, U. Anselmi-Tamburini, Self-propagating exothermic reactions: the synthesis of high-temperature materials by combustion, *Mater. Sci. Rep.* 3 (1989) 277–365.
- [31] T. Wc, D. Hh, G. Hc, Effect of an SiC addition on the oxidation of ZrB₂, *Am. Ceram. Soc. Bull.* 52 (1973) 612–616.
- [32] D. Sciti, L. Silvestroni, M. Nygren, Spark plasma sintering of Zr- and Hf-borides with decreasing amounts of MoSi₂ as sintering aid, *J. Eur. Ceram. Soc.* 28 (2008) 1287–1296.
- [33] E. Sani, D. Sciti, L. Silvestroni, A. Bellucci, S. Orlando, D.M. Trucchi, Tailoring optical properties of surfaces in wide spectral ranges by multi-scale femtosecond-laser texturing: a case-study for TaB₂ ceramics, *Opt. Mater.* 109 (Nov. 2020), <https://doi.org/10.1016/j.optmat.2020.110347>.
- [34] E. Sani, D. Sciti, S. Failla, C. Melandri, A. Bellucci, D. Trucchi, Multi-Scale femtosecond-laser texturing for photothermal efficiency enhancement on solar absorbers based on TaB₂ ceramics, *Nanomaterials* 13 (2023) 1692, <https://doi.org/10.3390/nano13101692>.
- [35] H.M. Cekirge, S.E. Erturan, R.S. Thorsen, The CSP (concentrated solar power) plant with brayton cycle: a third generation CSP system, *Am. J. Mod. Energy* 6 (2020) 43–50.
- [36] J. Karni, A. Kribus, R. Rubin, P. Doron, The 'porcupine': a novel high-flux absorber for volumetric solar receivers, *J. Sol. Energy Eng.* 120 (1998) 85–95.
- [37] E. Sani, S. Failla, D. Sciti, Dark alumina for novel solar receivers, *Scripta Mater.* 176 (2020) 58–62, <https://doi.org/10.1016/j.scriptamat.2019.09.038>.

- [38] S. Failla, E. Sani, D. Sciti, Lightweight Alumina-B4c Composites for Structural and Functional Applications, 2024 submitted for publication.
- [39] C. Azina, S. Badie, A. Litnovsky, L. Silvestroni, E. Sani, J. Gonzalez-Julian, Optical properties and corrosion resistance of Ti2AlC, Ti3AlC2, and Cr2AlC as candidates for concentrated solar power receivers, Sol. Energy Mater. Sol. Cells 259 (2023) 112433.
- [40] B. Belgasim, Y. Aldali, M.J. Abdunnabi, G. Hashem, K. Hossin, The potential of concentrating solar power (CSP) for electricity generation in Libya, Renew. Sustain. Energy Rev. 90 (2018) 1–15.